J. Fluid Mech. (2007), *vol.* 586, *pp.* 449–464.
doi:10.1017/S0022112007007021 Printed in the United Kingdom

Sedimenting sphere in a variable-gap Hele-Shaw cell

ANDREW T. LEE[1], EDUARDO RAMOS[1,2] AND HARRY L. SWINNEY[1]

[1]Center for Nonlinear Dynamics and the Department of Physics, University of Texas at Austin, Austin, TX 78712, USA

[2]Centro de Investigación en Energía, Universidad Nacional Autónoma de México, Ap.P. 34, 62580 Temixco Mor, México

(Received 27 January 2005 and in revised form 24 April 2007)

We have measured the trajectory and visualized the wake of a single sphere falling in a fluid confined between two closely spaced glass plates (a Hele-Shaw cell). The position of a sedimenting sphere was measured to better than $0.001d$, where d is the sphere diameter, for Reynolds numbers (based on the terminal velocity) between 20 and 330, for gaps between the plates ranging from $1.014d$ to $1.4d$. For gaps in the range $1.01d$–$1.05d$, the behaviour of the sedimenting sphere is found to be qualitatively similar to that of an unconfined cylinder in a uniform flow, but our sedimenting sphere begins to oscillate and shed von Kármán vortices for $Re > 200$, which is far greater than the $Re = 49$ for the onset of vortex shedding behind cylinders in an open flow. When the gap is increased to $1.10d$–$1.40d$, the vortices behind the sphere are different – they are qualitatively similar to those behind a sphere sedimenting in the absence of confining walls. Our precision measurements of the velocity of a sedimenting sphere and the amplitude and frequency of the oscillations provide a benchmark for numerical simulations of the sedimentation of particles in fluids.

1. Introduction

The motion of blunt bodies in a fluid has been studied since the early days of the development of fluid mechanics. Even now sedimenting bodies yield surprising discoveries and challenges for theoretical analyses, but there have been few experiments using modern imaging techniques to examine a sedimenting body.

We have examined the sedimentation of a single sphere in a fluid contained between vertical plates separated by a distance only slightly greater than the sphere diameter. We focus on the flow dependence on the separation between the plates. We make measurements for Reynolds numbers ranging from about 30 to 300, but we do not examine in detail the values of the Reynolds numbers corresponding to successive bifurcations. We measure the sphere position in a co-moving reference frame and obtain high-precision results for the sphere velocity and the properties of the wake. Our results for the sphere terminal velocity should long serve as a benchmark for algorithms designed for the difficult general problem of numerical simulation of the Navier–Stokes equation in a system with moving boundaries.

Our observations reveal some qualitative features that are common to bodies sedimenting in the absence of sidewalls, and to flow past a fixed sphere or a fixed cylinder in unconfined geometries. Hence we review these situations in the following section.

We now define our notation. The x-axis is in the vertical direction, increasing in the direction of gravity; the y-axis is in the horizontal direction, parallel to the confining glass plates; and the z-axis is in the horizontal direction, perpendicular to the glass plates. The ratio of the distance between the sidewalls d_{gap} to the diameter of the sphere d is $\Gamma = d_{gap}/d$. After a sphere is released, it reaches a terminal velocity u_t, as defined in §4; the corresponding Reynolds number is $Re = du_t/\nu$, where ν is the kinematic viscosity of the fluid. For Re greater than a critical value, the sphere oscillates; the oscillations are characterized by the non-dimensional Strouhal frequency, $St = fd/u_t$, where f is the oscillation frequency. We also use the Galileo number, $G = (|\rho_p/\rho_f - 1|g)^{1/2}d^{3/2}/\nu$, where ρ_p and ρ_f are the particle and fluid densities, respectively, and g is the gravitational acceleration.

2. Related work

2.1. *Free sphere*

The terminal velocity of an unconfined sedimenting sphere was measured by Nakamura (1976) and by Clift, Grace & Weber (1978) but has not been the focus of more recent studies. Nakamura (1976) also observed an attached recirculating eddy behind a sedimenting sphere for $10 < Re < 190$, and Clift *et al.* (1978) described a transition where the wake becomes oscillatory at $Re \approx 130$. Simulations by Pan (1999) found that for $Re > 135$, a sphere falls with a spiral trajectory. This spiral motion has also been observed for the same Re in experiments on rising spheres (Karamanev & Nikolov 1992). For $Re > 200$, the wake develops a pair of bound counter-rotating vortex threads (Jenny, Dusek & Bouchet 2004), and for $Re > 270$, the vortex threads are shed in pairs behind the sphere as it descends (Clift *et al.* 1978); simulations yield $St = 0.176$ for the shedding frequency (Jenny *et al.* 2004). For larger Reynolds number, the trajectory of the sphere depends strongly on its density relative to the fluid. If the sphere density is smaller than about one-third the fluid density, the sphere ascends in zigzagging or irregular spiral trajectory (Karamanev & Nikolov 1992). The irregular spiral motion is a consequence of the time-dependent forces that act on a sphere when the wake is unstable; the Strouhal number coincides with that of the unstable wake for fixed spheres (Karamanev 1994; Karamanev, Chavarie & Mayer 1996; Karamanev & Nikolov 1992). If the density of a sphere is comparable with or larger than the density of the fluid, the wake structure is similar to that of a fixed sphere (see the following subsection).

2.2. *Fixed sphere*

The fixed sphere problem is simpler than a free sphere because there is no motion of the sphere to affect the flow, and Re is set by the imposed free-stream velocity. For $Re > 24$ the boundary layer detaches, and a steady toroidal vortex forms behind the sphere (Taneda 1956; Johnson & Patel 1998). The longitudinal extent of this vortex increases with Reynolds number, and at about $Re = 200$ the flow bifurcates to a non-axisymmetric flow with two parallel counter-rotating vortex tubes attached to the recirculation region on opposite sides of the sphere and extending downstream; this flow pattern has a plane of symmetry perpendicular to the plane containing the vortex tube centres. The critical Reynolds number obtained in a linear stability analysis by Natarajan & Acrivos (1993) was 210, while direct numerical simulations by Tomboulides & Orszag (2000) and Johnson & Patel (1998) gave 212 and 211, respectively, and an experiment by Ormieres & Provansal (1999) yielded 180. At

$Re \approx 270$, the parallel vortex tubes begin to form hairpin vortices that are periodically swept away. Schouveiler & Provansal (2002) interpreted this phenomenon in terms of the Crow vortex pair instability (Crow 1970; Widnall, Bliss & Zalay 1971) and established that this transition occurs with no hysteresis and with a well-defined frequency, $St = 0.127$. Ormieres & Provansal (1999) observed the vortical structure and stability in the proximity of this transition. Numerical simulations by Tomboulides & Orszag (2000), Johnson & Patel (1998), and Lee (2000) agree with the experimental observations and provide a detailed description of the motion. In the Reynolds number range 270–370, vortex shedding still displays a planar symmetry, and oppositely oriented hairpin vortices are generated. This double-sided wake structure arises from the one-sided vortex shedding and the interaction of the free stream with the shed vortices (Johnson & Patel 1998). At $Re \approx 370$, the planar symmetry is lost, and the wake develops a low-frequency modulation (Mittal 2000).

2.3. *Fixed cylinder*

Experimental and theoretical studies of flow past a long cylinder (at a large distance from sidewalls) have been reviewed by Zdravkovich (1997, 2002), and Williamson (1996). Coutanceau & Defaye (1991) observed an attached recirculation zone that formed at the rear of a cylinder for $4.5 < Re < 35$; Williamson (1996) described this regime as laminar steady flow with two symmetric recirculation vortices attached to the cylinder. The length of the vortex pair increases with the Reynolds number, and at $Re = 35$ the width of the recirculation zone is about the same size as the cylinder diameter. The recirculation zone becomes unstable at $Re = 46$. These transitions were described differently by Zdravkovich (1997), who considered fluctuations in the behaviour of the entire system as the main indicator of transitions. Beyond $Re \approx 50$ the far downstream point of the recirculation region develops instabilities, and the wake behind the cylinder begins to shed vortices from alternate sides of the recirculation zone. These alternating two-dimensional von Kármán vortices have axes of rotation parallel or slightly oblique to the axis of the cylinder. Simulations (Mittal 2001) and experiments (Hover, Techet & Triantafyllou 1998) in this regime show that the forces felt by the cylinder are periodic and coincide with the shedding of vortices. The Strouhal number increases continuously and monotonically from 0.12 to 0.19 in the range $49 < Re < 180$, where vortices are shed from the cylinder parallel or slightly obliquely to the cylinder axis. At higher Re, three-dimensional effects become increasingly important.

3. Experimental methods

Our experiment was designed to track precisely the position of a single sphere sedimenting in a Newtonian fluid in a Hele-Shaw cell. The cell was constructed of two glass plates that were parallel to the gravitational force. The two glass plates were 1.27 cm thick, 60 cm high, and 25 cm wide, and were separated by precision-ground stainless steel spacers that yielded gap-to-ball-diameter ratios $\Gamma = (1.014, 1.044, 1.101, 1.201, 1.401) \pm 0.003$.

Glass spheres of high sphericity had a diameter $d = 0.3175 \pm 0.0003$ cm, and densities $\rho_p = 2.52 \pm 0.02\ \mathrm{g\,cm^{-3}}$ (Winsted Precision Ball Company) and $3.07 \pm 0.02\ \mathrm{g\,cm^{-3}}$ (Sapphire Engineering). (The densities of the glass spheres were determined by measuring the total mass of five balls with a precision scale.) Measurements were made using one sphere of each material for each cell configuration.

The desired range of Reynolds number, $20 < Re < 300$, was achieved using dense aqueous neutral solutions of an inert salt, sodium metatungstate ($Na_6H_2W_{12}O_{40}$), obtained from Sometu-USA (www.sometu.com). We prepared fluid solutions with densities in the range $1 < \rho_f < 2.5\,\mathrm{g\,cm^{-3}}$, while the kinematic viscosity $\nu = \mu/\rho_f$ varied in the range 0.013–$0.025\,\mathrm{cm^2\,s^{-1}}$. The experiment was operated at room temperature, which was recorded for each measurement. The viscosity of a $1.93\,\mathrm{g\,cm^{-3}}$ sodium metatungstate solution was measured with a cone-and-plate viscometer for shear rates ranging from 100 to $1500\,\mathrm{s^{-1}}$, and was found to be a constant $1.30\,\mathrm{cm^2\,s^{-1}}$ (at 25 °C) within the 2 % uncertainty of the measurements; hence non-Newtonian effects should be negligible.

To determine the terminal velocity and measure small fluctuations of the sphere position (at most $\sim 10^{-2}d$) with high positional precision, we followed the motion of the sphere in the co-moving frame as the sphere fell many diameters. A sphere was tracked in the horizontal and vertical directions; motion in the direction perpendicular to the plates was not determined. A 60 frames per second, 776×576 pixel CCD camera was mounted on a vertical translation stage that followed a sphere at approximately its terminal velocity. To correct for the small relative drift between the camera and the sphere as well as for the vibrations of the moving camera, a row of stationary reference marks was imaged throughout the vertical path of the camera. Illumination was provided by a red LED array; the light passed through a plastic diffusion screen.

The trajectory of the camera was determined using the relative positions of the reference marks from image to image. This gave the trajectory of the camera with sub-pixel accuracy. Additional care was taken to account for any tilt in the mounting of the camera. A thin wire was attached to a mass and imaged to determine the direction of gravity relative to the camera mount.

The position of a sphere was tracked in each image of a series of images. The sphere was illuminated from behind and appeared as a dark circular feature approximately 80 pixels in diameter. Each image was analysed using a centre-of-mass particle tracking method adapted from Crocker & Grier (1996). The sphere position in each image and the positions of stationary reference marks were calculated using the same algorithm, and the absolute vertical position was found by integrating the motion of the camera over its entire path relative to reference marks. The first moment of the intensity distribution corresponding to a sphere was calculated with sub-pixel accuracy and was taken to correspond to the centre of the sphere.

The centre-of-mass tracking algorithm resolved motion as small as $10^{-3}d$ ($\sim 3\,\mu\mathrm{m}$) over a sedimentation distance of $150d$. The measurements yielded Re, the time-dependence of the fluctuations in the transverse (y) and gravitational (x) directions, and the corresponding oscillation frequencies, f_y and f_x.

We characterized the wake of the sphere using digital particle image velocimetry (DPIV) synchronized with our particle tracking system. For the cases where DPIV measurements were made, the fluid was seeded with $10\,\mu\mathrm{m}$ silver-coated glass spheres, and the particle imaging camera was fitted with a red filter so that images used for particle tracking would be sensitive only to the position of the subject sphere. Additionally, during these DPIV measurements, a second camera imaging at 1016×1008 pixels at 15 frames per second was mounted beside the particle imaging camera. Although the DPIV camera imaged at 15 frames per second, each frame consisted of two images separated by a set amount of time (400–800 μs), depending on the terminal velocity of the sphere. This camera was fitted with a green filter for use with a YAG laser. Illumination from above was then applied using a pulsed YAG laser sheet. The green laser sheet scattered light from the silver-coated spheres so that

DPIV images could be obtained using the second camera. During an experimental measurement, the particle tracking camera would detect the motion of the sphere and then trigger the DPIV camera to begin synchronous image capturing.

Each set of images was analysed using the algorithm MatPIV.† The algorithm uses cross-correlation PIV and an iterative interrogation window to calculate the velocity and vorticity fields of the fluid flow. The final interrogation window size was 16×16 pixels or 0.06×0.06 cm.

After filling the cell with the aqueous solution of choice, a glass sphere was held in position by a tube at a pressure below atmospheric. After the sphere was released, the camera was set into motion and images were recorded. Multiple measurements were made for the same sphere.

After each series of measurements, the density ρ_f of the sodium metatungstate solution was measured using a Gay-Lussac bottle with a calibrated volume of 10.00 ± 0.03 ml to obtain a known volume whose mass could then be measured. This measurement was repeated three times for each solution. Immediately following a set of experimental measurements, a sample of the solution was injected into a Cannon-Fenske capillary viscometer and the efflux time for the solution to fall under the influence of gravity was measured. The calibrated viscosity was found by multiplying the efflux time by the viscometer constant. The viscosity measurement was repeated three times per fluid sample. Following each viscosity measurement, the viscometer was cleaned with distilled water and isopropanol and then dried with nitrogen to remove all traces of the solution.

We made 10–20 observations for five different gap configurations for a variety of fluid densities. This provided over 800 single-particle measurements. DPIV data were obtained for a few cases that exhibited oscillatory behaviour; for these selected cases DPIV and particle trajectory measurements were made simultaneously.

4. Data analysis

After a sphere was released, it reached its terminal velocity within a distance of typically $5d$, and its asymptotic motion was then followed for a distance of about $150d$. The position of the camera was determined as a function of time in both the vertical (gravitational, x) and transverse (y) directions, and then the sphere trajectory was calculated relative to its starting position. After the sphere has reached 99 % of the mean maximum velocity, its position $x(t)$ was fitted to a line to obtain the terminal velocity, u_t, which was used to find Re. The mean motion was subtracted to yield the fluctuations in $x(t)$, while the transverse position $y(t)$ was determined directly.

The trajectory of a sphere was measured for five different gap distances. For each experimental condition the terminal velocities were averaged to obtain u_t with statistical uncertainty less than 1 %. A post-transient trajectory for $Re = 125$ is shown in figure 1. For this case the sphere reached 99 % of its terminal velocity within 0.5 s. The motion of the sphere in the average co-moving frame is shown in figure 1, and the position $x(t)$ in the laboratory frame is shown in the inset.

The frequencies of periodic oscillation were obtained from Fourier transforms of the co-moving positions as a function of time, $x(t)$ and $y(t)$ (each filtered using a triangular windowing method). The amplitudes of the oscillation were obtained directly from position data that had been bandpass filtered at the oscillation frequency.

† http://www.math.uio.no/~jks/matpiv/

Conditions				Experimental results					
$\frac{\rho_p}{\rho_f}$	ρ_p (g cm^{-3})	ρ_f (g cm^{-3})	ν (cm^2 s^{-1})	u_t (cm s^{-1})	Re	A_x (d)	St_x	A_y (d)	St_y
1.151	2.523	2.193	0.01695	4.46 ± 0.03	84 ± 1	–	–	–	–
1.167	2.523	2.162	0.01607	4.88 ± 0.05	96 ± 1	–	–	–	–
1.192	2.523	2.117	0.01521	5.47 ± 0.06	114 ± 2	–	–	–	–
1.188	2.523	2.123	0.01538	5.70 ± 0.13	118 ± 3	–	–	–	–
1.219	2.523	2.070	0.01431	6.28 ± 0.07	139 ± 2	–	–	–	–
1.243	2.523	2.030	0.01398	6.90 ± 0.07	157 ± 2	–	–	–	–
1.274	2.523	1.980	0.01294	7.35 ± 0.05	180 ± 2	–	–	–	–
1.401	3.073	2.193	0.01695	8.67 ± 0.04	162 ± 1	–	–	–	–
1.422	3.073	2.162	0.01607	9.07 ± 0.07	179 ± 2	–	–	–	–
1.451	3.073	2.117	0.01521	9.62 ± 0.06	201 ± 2	–	–	–	–
1.447	3.073	2.123	0.01538	9.68 ± 0.12	200 ± 3	–	–	–	–
1.484	3.073	2.070	0.01431	10.22 ± 0.18	227 ± 4	–	–	–	–
1.514	3.073	2.030	0.01398	10.75 ± 0.11	244 ± 3	–	–	0.016 ± 0.006	0.130
1.552	3.073	1.980	0.01294	11.30 ± 0.06	277 ± 3	–	–	0.071 ± 0.006	0.141

TABLE 1. Results and experimental conditions for gap ratio $\Gamma = 1.014$.

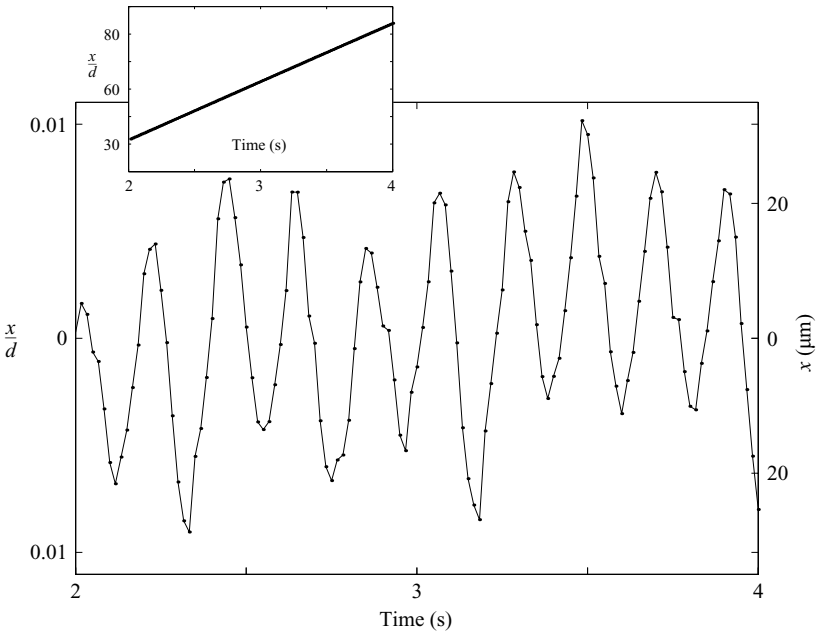

FIGURE 1. The vertical position of a particle in a reference frame moving with the terminal velocity. In this frame the amplitude of oscillations is less than 1 % d, yet the noise level of the data is less than 0.1 % d. Inset: The terminal velocity was obtained from a linear fit of post-transient data for $x(t)$ in the laboratory frame. $\Gamma = 1.30$, $Re = 125$.

5. Results

5.1. *Overview*

The data are presented in tables 1–5. Figure 2 shows the different regimes of motion that were observed for different gap sizes Γ. At low Re the motion was time

Conditions				Experimental results					
$\frac{\rho_p}{\rho_f}$	ρ_p (g cm^{-3})	ρ_f (g cm^{-3})	ν (cm^2 s^{-1})	u_t (cm s^{-1})	Re	A_x (d)	St_x	A_y (d)	St_y
1.108	2.523	2.278	0.01831	3.48 ± 0.03	60 ± 1	–	–	–	–
1.132	2.523	2.230	0.01782	4.11 ± 0.03	73 ± 1	–	–	–	–
1.153	2.523	2.187	0.01640	4.76 ± 0.05	92 ± 1	–	–	–	–
1.192	2.523	2.117	0.01536	5.67 ± 0.06	117 ± 2	–	–	–	–
1.221	2.523	2.067	0.01454	6.38 ± 0.04	139 ± 1	–	–	–	–
1.349	3.073	2.278	0.01831	7.87 ± 0.07	136 ± 2	–	–	–	–
1.378	3.073	2.230	0.01782	8.48 ± 0.07	151 ± 2	–	–	–	–
1.405	3.073	2.187	0.01640	8.90 ± 0.04	172 ± 1	–	–	–	–
1.452	3.073	2.117	0.01536	9.84 ± 0.08	203 ± 2	–	–	–	–
1.487	3.073	2.067	0.01454	10.42 ± 0.09	228 ± 3	–	–	0.004 ± 0.002	0.126

TABLE 2. Results and experimental conditions for gap ratio $\Gamma = 1.044$.

Conditions				Experimental results					
$\frac{\rho_p}{\rho_f}$	ρ_p (g cm^{-3})	ρ_f (g cm^{-3})	ν (cm^2 s^{-1})	u_t (cm s^{-1})	Re	A_x (d)	St_x	A_y (d)	St_y
1.047	2.523	2.409	0.02434	1.99 ± 0.01	26 ± 1	–	–	–	–
1.072	2.523	2.354	0.02252	3.09 ± 0.01	44 ± 1	–	–	–	–
1.109	2.523	2.275	0.01939	4.25 ± 0.05	70 ± 1	–	–	–	–
1.146	2.523	2.202	0.01772	5.54 ± 0.04	99 ± 1	–	–	–	–
1.219	2.523	2.070	0.01450	7.83 ± 0.02	172 ± 1	–	–	–	–
1.259	2.523	2.004	0.01343	8.92 ± 0.01	211 ± 1	–	–	–	–
1.227	3.073	2.504	0.02978	6.26 ± 0.01	67 ± 1	–	–	–	–
1.276	3.073	2.409	0.02434	7.78 ± 0.01	102 ± 1	–	–	–	–
1.306	3.073	2.354	0.02252	8.65 ± 0.02	122 ± 1	–	–	–	–
1.351	3.073	2.275	0.01939	9.90 ± 0.01	162 ± 1	–	–	–	–
1.395	3.073	2.202	0.01772	11.00 ± 0.01	197 ± 1	–	–	–	–
1.485	3.073	2.070	0.01450	12.95 ± 0.04	284 ± 1	–	–	0.015 ± 0.003	0.120
1.534	3.073	2.004	0.01343	13.91 ± 0.02	329 ± 1	–	–	0.024 ± 0.003	0.120

TABLE 3. Results and experimental conditions for gap ratio $\Gamma = 1.101$.

Conditions				Experimental results					
$\frac{\rho_p}{\rho_f}$	ρ_p (g cm^{-3})	ρ_f (g cm^{-3})	ν (cm^2 s^{-1})	u_t (cm s^{-1})	Re	A_x (d)	St_x	A_y (d)	St_y
1.067	2.523	2.364	0.02302	3.08 ± 0.02	42 ± 1	–	–	–	–
1.104	2.523	2.286	0.01998	4.47 ± 0.01	71 ± 1	–	–	–	–
1.164	2.523	2.168	0.01595	6.60 ± 0.02	131 ± 1	–	–	–	–
1.185	2.523	2.129	0.01488	7.34 ± 0.03	157 ± 1	0.005 ± 0.002	0.245	0.003 ± 0.001	0.124
1.300	3.073	2.364	0.02302	8.97 ± 0.01	124 ± 1	–	–	0.001 ± 0.001	0.123
1.344	3.073	2.286	0.01998	10.15 ± 0.03	161 ± 1	0.006 ± 0.001	0.239	0.004 ± 0.001	0.119
1.418	3.073	2.168	0.01595	11.84 ± 0.02	236 ± 1	0.012 ± 0.004	0.127	0.004 ± 0.001	0.126
1.444	3.073	2.129	0.01488	12.40 ± 0.03	265 ± 1	0.025 ± 0.005	0.128	0.003 ± 0.001	0.128

TABLE 4. Results and experimental conditions for gap ratio $\Gamma = 1.201$.

Conditions				Experimental results					
$\frac{\rho_p}{\rho_f}$	ρ_p (g cm^{-3})	ρ_f (g cm^{-3})	ν (cm^2 s^{-1})	u_t (cm s^{-1})	Re	A_x (d)	St_x	A_y (d)	St_y
1.043	2.523	2.418	0.02438	2.36 ± 0.01	31 ± 1	–	–	–	–
1.106	2.523	2.282	0.01951	5.07 ± 0.02	83 ± 1	–	–	–	–
1.152	2.523	2.190	0.01693	6.67 ± 0.02	125 ± 1	0.011 ± 0.001	0.225	0.007 ± 0.001	0.112
1.185	2.523	2.128	0.01496	7.68 ± 0.02	163 ± 1	0.016 ± 0.002	0.222	0.007 ± 0.001	0.111
1.219	2.523	2.070	0.01436	8.64 ± 0.02	191 ± 1	0.018 ± 0.002	0.222	0.006 ± 0.001	0.111
1.266	2.523	1.993	0.01307	9.97 ± 0.03	242 ± 1	0.041 ± 0.004	0.113	0.009 ± 0.002	0.113
1.271	3.073	2.418	0.02438	8.81 ± 0.02	115 ± 1	0.008 ± 0.002	0.224	0.007 ± 0.001	0.112
1.347	3.073	2.282	0.01951	10.90 ± 0.03	177 ± 1	0.013 ± 0.003	0.214	0.006 ± 0.001	0.107
1.403	3.073	2.190	0.01693	12.25 ± 0.01	230 ± 1	0.020 ± 0.001	0.109	0.007 ± 0.001	0.109
1.444	3.073	2.128	0.01496	13.23 ± 0.02	281 ± 1	0.022 ± 0.005	0.109	0.007 ± 0.001	0.110
1.485	3.073	2.070	0.01436	15.06 ± 0.40	333 ± 9	0.044 ± 0.029	0.077	0.004 ± 0.002	0.069

TABLE 5. Results and experimental conditions for gap ratio $\Gamma = 1.401$.

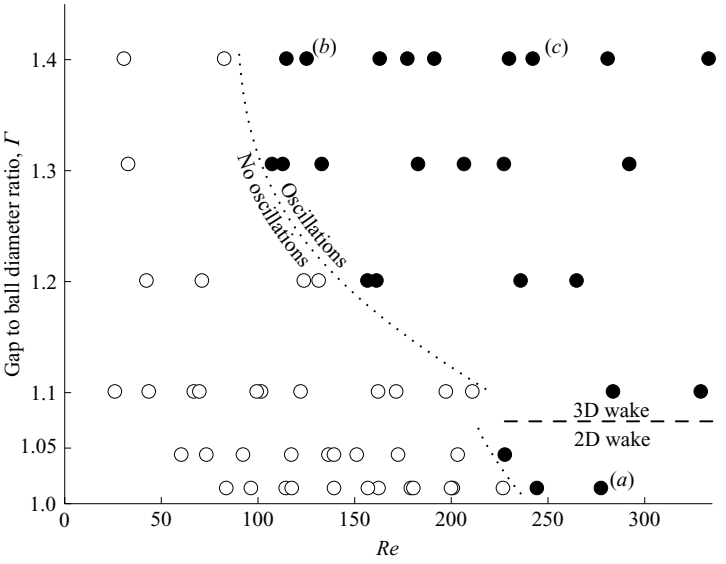

FIGURE 2. Different regimes of motion and the wake structure observed for a sedimenting sphere between closely spaced plates. Reynolds numbers Re were found from particle tracking, while wake types were determined from DPIV images of the flow following the sphere. The dotted line (drawn to guide the eye) separates regions with no discernible periodic behaviour (left, unfilled circles) from regions with oscillatory behaviour (right, filled circles). In the region below the horizontal dashed line, the wake is essentially two-dimensional, and in the remainder of the diagram is three-dimensional. The time dependence of trajectories of three cases labelled (a),(b), and (c) is shown in figure 3.

independent, and at sufficiently large Re the motion was oscillatory. For our largest gap ($\Gamma = 1.4$) the onset of oscillatory behaviour occurred between $Re = 83$ and $Re = 125$, while for our smallest gap ($\Gamma = 1.014$), this transition occurred between $Re = 227$ and $Re = 244$.

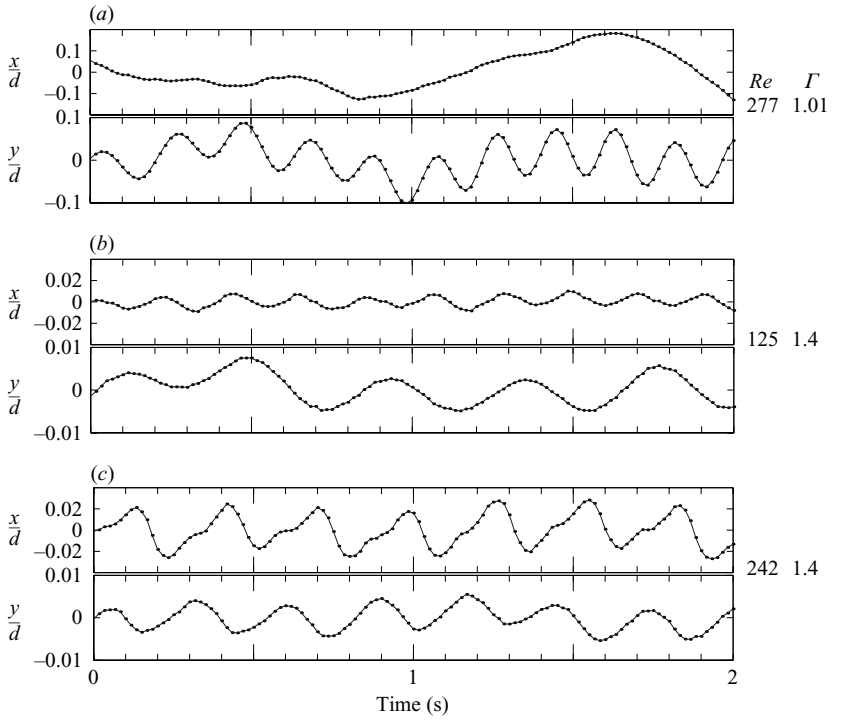

FIGURE 3. Vertical (x) and transverse horizontal (y) components of the position of a sedimenting sphere with respect to the average co-moving reference frame for three cases. (a) The transverse oscillation amplitude for $\Gamma = 1.014$ is greater than for $\Gamma = 1.4$, shown in (b) and (c). The trajectory for (a) in the vertical direction does not exhibit regular periodic motion, while trajectories for $\Gamma = 1.4$ exhibit periodic oscillations at twice the frequency of the transverse oscillation (low Re, (b)) and at the same frequency of the transverse motion (high Re, (c)).

Most trajectories exhibited a small irregular transverse drift that was not monotonic, as illustrated in figure 3(a). This drift was different for drops under the same conditions, but it was always irregular and small, typically less than $0.5d$ over the $150d$ trajectory length. This drift was removed from our figures.

The points in figure 2 labelled (a), (b), and (c) represent the three most common types of observed oscillatory behaviour. Figure 3(a) shows the trajectory of a falling sphere with $\Gamma = 1.014$ (two-dimensional wake). In the co-moving reference frame the position of the sphere in the gravitational direction during the entire fall deviated from the centre of the frame by less than 10 % of a sphere diameter; this deviation did not contain any discernible periodic pattern. In the transverse direction y, the sphere exhibited oscillatory behaviour. For the larger gap ($\Gamma = 1.401$, three-dimensional wake) in figures 3(b) and 3(c), the oscillation amplitude was smaller. In figure 3(b) ($Re = 125$), the frequency of oscillation in the x-direction was twice the frequency of oscillation in the y-direction, while for figure 3(c), where $Re = 242$, the frequencies of oscillation in the x-and y-directions were equal.

There is a gradual transition with increasing Re from the type of $x(t)$ trajectory in figure 3(b) to that in figure 3(c). At small Re, Fourier spectra of $x(t)$ contain both St_y and $2St_y$ but $2St_y$ is dominant. As Re is increased, the two components become equal in strength and eventually the dominant frequency component in $x(t)$ becomes St_y.

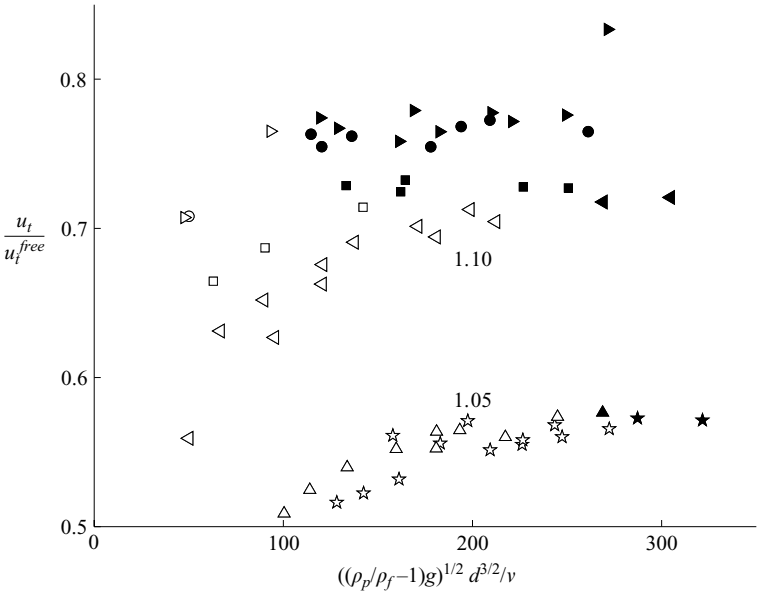

FIGURE 4. The distinction between particles with a quasi-two-dimensional wake ($\Gamma \leqslant 1.05$) and a three-dimensional wake ($\Gamma \geqslant 1.10$) is apparent in this comparison of the terminal velocity u_t of a sedimenting sphere in a Hele-Shaw cell with the velocity u_t^{free} of a sphere without confining sidewalls. The symbols indicate the gap-to-sphere-diameter ratio (★, $\Gamma = 1.01$; ▲, $\Gamma = 1.05$; ◄, $\Gamma = 1.10$; ■, $\Gamma = 1.20$; ●, $\Gamma = 1.30$; ►, $\Gamma = 1.40$); unfilled points indicate time-independent motion and filled points indicate periodic trajectories.

5.2. *Terminal velocity*

In figure 4 we compare our terminal velocity values u_t with the velocities u_t^{free} for free sedimenting spheres. For u_t^{free} we use an expression that Clift *et al.* (1978) found to fit available data for unconfined sedimenting spheres within 4 % for $12.2 < Re < 6350$,

$$\log_{10} Re = -1.81391 + 1.34671W - 0.12427W^2 + 0.006344W^3, \tag{5.1}$$

where $W = \log_{10}(\frac{4}{3}G)$. Our results for u_t/u_t^{free} separate into two distinct groups; a small gap case ($\Gamma \leqslant 1.05$), where the terminal velocities approach an asymptotic value less than 55 % of that of free spheres, and a larger gap case ($1.1 \leqslant \Gamma \leqslant 1.4$), where the terminal velocities are larger but asymptotically still at most 75 % of that of free spheres.

5.3. *Wake structure*

The structures of the wakes behind the oscillating spheres for conditions in figure 3 are shown in figure 5. (Wakes measured for cases without oscillation did not exhibit significant structure.) For $\Gamma = 1.014$ (figure 5*a*), the von Kármán vortex structure of the wake can be seen clearly in the two magnified plots; note that the Reynolds number (277) is well above the value 220 that corresponds to the onset of vortex shedding. As a vortex is shed, the sphere begins to move in the opposite transverse direction.

In figure 5(*b*) the gap distance is 40 % larger than the diameter of a sphere and *Re* is slightly above the onset of oscillations for this gap size. A sphere creates two three-dimensional trailing structures during the fall. For a larger *Re* (figure 5*c*), the sphere sheds vortices. The time sequence of images shows that a vortex pair that is

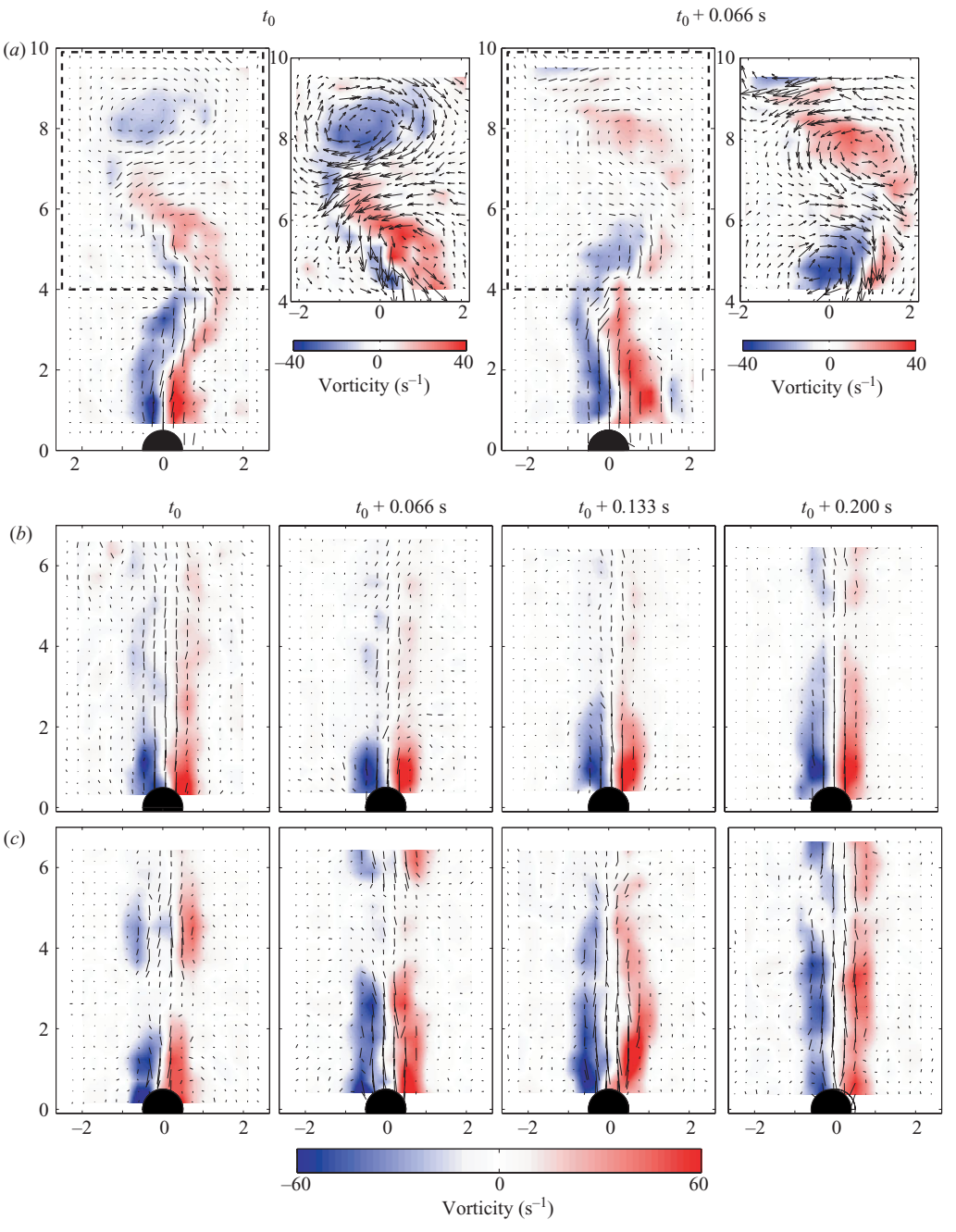

FIGURE 5. Flow field images at multiple times for the same conditions as in figure 3. Velocity values are indicated by the line segments and vorticity values by background colours. For reference the sphere is shown as a black circle. In the small-gap case (*a*), the regions in dashed boxes (each magnified in vorticity in a box to their right) show von Kármán vortices at different points during a cycle.

created at time t_0 is carried away from the sphere and a new vortex pair is created. The shedding frequencies in figures 5(*b*) and 5(*c*) are the same as the corresponding frequencies for the trajectory motion (figures 3*b* and 3*c*).

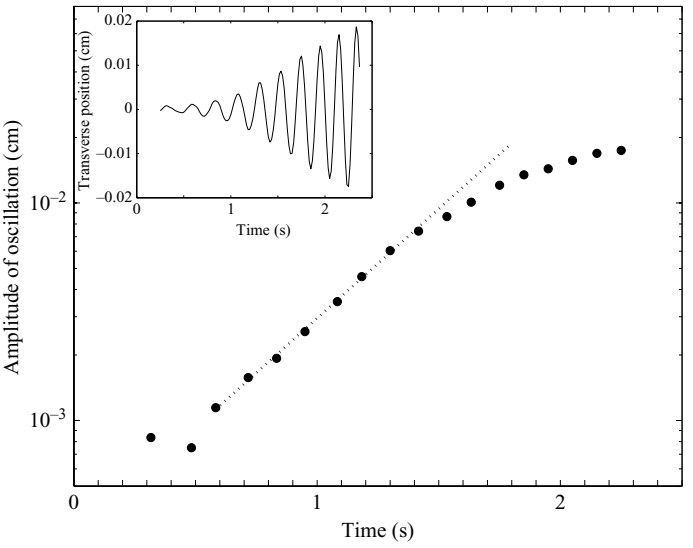

FIGURE 6. The amplitude of oscillations grows exponentially at a rate of $8.14\,\mathrm{s}^{-1}$ ($\Gamma = 1.014$, $Re = 277$). Inset: The oscillatory trajectory of the sphere corresponding to the amplitude measurement.

5.4. $\Gamma \leqslant 1.05$

For $60 < Re < 230$, trajectories exhibited small, slow aperiodic variations. At $Re = 230$, a falling sphere began to exhibit periodic transverse oscillations, which were superposed on the slow aperiodic oscillations observed at smaller Re; no vertical oscillation was discernible. The transverse oscillations correspond to the creation and shedding of counter-rotating von Kármán vortices, as seen in figure 5(*a*). The structure of the quasi-two-dimensional vortices is similar to that for flow past a cylinder. Our measurements of the oscillation amplitude yield an exponential growth followed by saturation (figure 6); similar behaviour has been found for flow past a fixed sphere Provansal, Schouveiler & Leweke (2004).

5.5. $1.1 \leqslant \Gamma \leqslant 1.4$

The transition from non-periodic to periodic behaviour observed for this case is indicated in figure 2 by the dotted line. We analysed the data using the method of Schouveiler & Provansal (2002), who measured for flow past a fixed sphere (without confining sidewalls) the fluctuations of the fluid velocity in the vertical direction directly behind the sphere. Schouveiler & Provansal (2002) determined that the energy of these fluctuations at the primary shedding frequency increased linearly with increasing Re, indicating that the transition was a supercritical Hopf bifurcation.

We measured the motion of the sphere (rather than the fluid velocity) and found that above the onset of oscillations, the average amplitude of the velocity fluctuations increased linearly with Re (figure 7). A linear fit to the data for $\Gamma = 1.30$ and 1.40 gives $Re = 89$ for this Hopf bifurcation.

For Re close to onset of oscillatory behaviour, a sphere oscillates in the vertical direction at twice the frequency of the transverse oscillations (see figure 3*b*). The spectral power at St_y and $2St_y$, plotted in figure 8(*a*), shows an evolution in behaviour with increasing Re: at large Re the mode St_y approaches 100 % of the power. This evolution is illustrated by the phase-space portraits in figure 8(*b*). At $Re = 125$ a

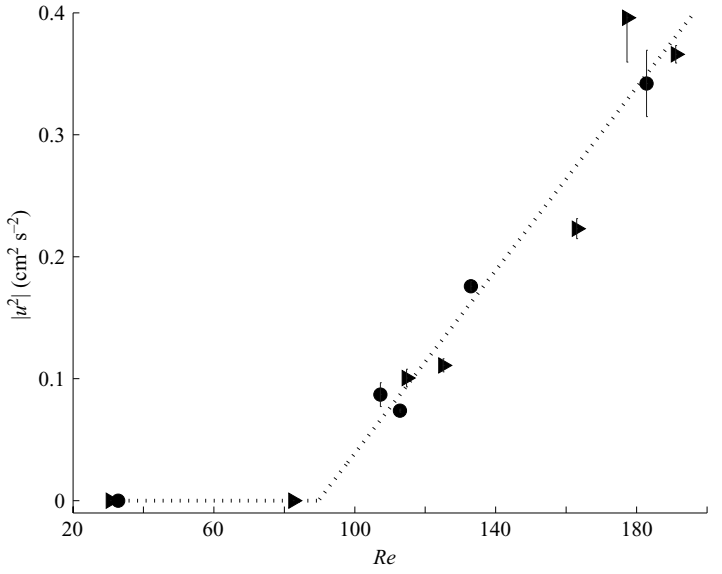

FIGURE 7. The square of the average amplitude of the velocity fluctuations, $u_x^2 + u_y^2$ (cm^2 s^{-2}), increases linearly with Re beyond the onset of oscillations. The graph includes measurements for $\Gamma = 1.30$ (●), and 1.40 (►).

sphere's motion is symmetric in the vertical and horizontal directions, while for larger Re, the motion becomes asymmetric as one lobe decreases in size and the opposite lobe increases. Eventually, the smaller lobe disappears completely.

6. Discussion

Our measurements on spheres of diameter d sedimenting in a Hele-Shaw cell used digital imaging to track a sphere's position with a precision better than $0.001d$ (tables 1–5), which is far better precision than previous experiments on sedimenting spheres. Further, information on the velocity field was obtained using particle imaging velocimetry. Our experiments examined particularly the dependence of the behaviour on Γ (the ratio of plate separation to d). The measurements revealed a clear distinction between the behaviour for spheres sedimenting for $1.014 \leqslant \Gamma \leqslant 1.044$, where the behaviour has qualitative similarities to flow past a fixed unconfined cylinder, and the behaviour for $1.10 \leqslant \Gamma \leqslant 1.40$, where the behaviour is qualitatively similar to that for an unconfined sedimenting sphere and for flow past a fixed sphere. A sedimenting sphere in a Hele-Shaw cell is a rather different problem from a sphere sedimenting without sidewalls, and from a fixed sphere or cylinder in a uniform flow, so no direct correspondence between our study and these other problems can be expected, but we mention some qualitative similarities in behaviour that are helpful in interpreting the observed phenomena.

For $\Gamma = 1.014$ and $\Gamma = 1.044$, the pattern of the vortices observed for $Re > 240$ is like the $2S$ configuration of flow past a cylinder observed by Jauvtis & Williamson (2004)(see also Govardhan & Williamson 2000), i.e. one vortex is shed per half-cycle of particle oscillation. For our sedimenting sphere, the amplitude of the transverse oscillation was at most $0.07d$, which was observed for particle-to-fluid density ratios $(\rho_p/\rho_f) = 1.5$ and $Re = 277$. In contrast, the amplitude of the transverse oscillation of a cylinder with similar density ratios is as large as $1.5d$ (for $Re \approx 5000$).

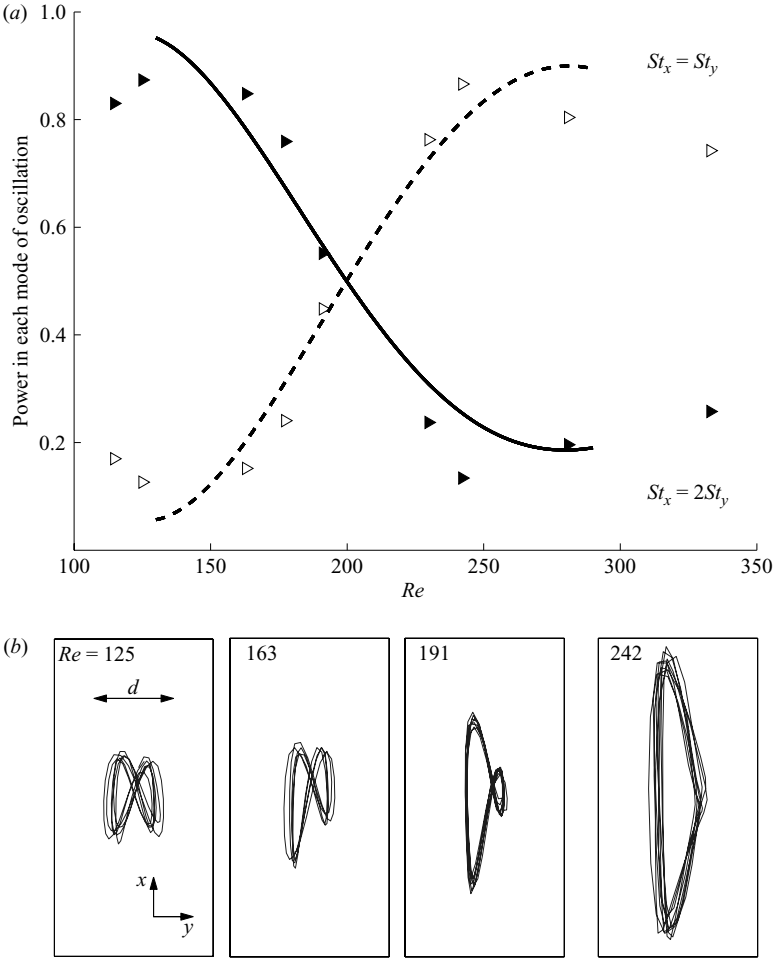

FIGURE 8. (*a*) The amplitude of the power spectrum for the trajectory of a sphere in the vertical direction for $\Gamma = 1.40$. For low Re the dominant component oscillates at twice the frequency of the oscillations in the transverse direction, but as Re increases, the component at the frequency of the transverse oscillation becomes dominant (▷, $St_x = St_y$; ▶, $St_x = 2St_y$). (*b*) The trajectory of a sphere (in its co-moving frame) shows the transition from the frequency-doubled vertical oscillation to the single-frequency oscillation at higher Re.

Further, for $\Gamma = 1.014$ and $\Gamma = 1.044$, as a sphere releases a clockwise (counter-clockwise) vortex, the sphere moves to the right (left) (cf. figure 5*a*). These observations are consistent with the analysis of Jauvtis & Williamson (2004) (see also Lighthill 1986), who suggested that the force exerted on the particle due to a vortex shed upward will generate a horizontal force given by

$$\boldsymbol{F}_v = \rho \boldsymbol{\Omega} \times \boldsymbol{U}_v, \tag{6.1}$$

where $\boldsymbol{F}_v$ is the vortex force, $\boldsymbol{\Omega}$ is the total vorticity, and $\boldsymbol{U}_v$ is the fluid velocity around the particle.

In the smallest gap that we studied, $\Gamma = 1.014$, the sphere's motion was time independent at $Re = 227$ and oscillatory at $Re = 244$; thus the onset of oscillations occurs at a much larger Re value than the 49 found for oscillations of flow past

a cylinder without sidewalls (Williamson 1996). Similarly, observations of flow past cylinders between end plates revealed that the critical Reynolds number increased as the aspect ratio (length/diameter) decreased, an effect attributed to the stabilizing effect of the walls on the flow (Norberg 1994; Lee & Budwig 1991).

Our measurements for different Γ and Re yielded Strouhal frequencies in the range 0.12–0.15, which covers the range observed for flow past unconfined cylinders (Williamson & Roshko 1988) and bubbles with density ratios larger than 2.5 (Jenny *et al.* 2004). For our largest plate separation, $\Gamma = 1.40$, we observed time-independent motion at $Re = 83$ and oscillatory motion at $Re = 125$ (table 5); this result can be compared to $Re = 135$ found for the onset of oscillations in a three-dimensional numerical simulation of a sphere sedimenting without sidewalls (Pan 1999). Further, the flow field and vorticity we observed for a sedimenting sphere with $\Gamma = 1.40$ (figure 5) were similar to the results obtained for the wake behind a sphere for $Re = 345$ (Schouveiler & Provansal 2002, figure 6). Our visualizations using Kaliroscope particles for $\Gamma = 1.20$ and $Re = 310$ (not shown here) reveal that the structure of the wake is composed of sequences of hairpin vortices akin to those observed in the wake of spheres (Schouveiler & Provansal 2002) and bubbles (Brucker 1999).

No previous study has examined sedimentation in a Hele-Shaw cell as a function of plate separation. Thus our results will serve as a guide and benchmark for future experiments and for direct numerical simulations of the Navier–Stokes equation for sedimenting spheres. Numerical simulations for this problem are difficult not only because of the moving boundary but also because of the wide range of spatial scales; for example, in our experiments with the smallest gap between the plates ($\Gamma = 1.014$), the distance between the sphere and a wall is $\sim$140 times smaller than the diameter of the sphere. Future experiments and simulations should investigate how the behaviour of a confined sphere evolves with increasing plate separation ($\Gamma > 1.4$) to that of an unconfined sphere. Further, our measurements examined sedimentation at only a few values of Re, so it would be interesting to study in detail the sequence of bifurcations that occurs as a function of Reynolds number.

We thank Roland Glowinski, Dan Goldman, Howard Hu, W. D. McCormick, and Tsorng-Whay Pan for helpful comments and suggestions. This work was supported by the Robert A. Welch Foundation Grant F-805 and the Office of Naval Research Quantum Optics Initiative. This project was initiated during a visit of Eduardo Ramos to the Center for Nonlinear Dynamics of the University of Texas. He is grateful for the Center's hospitality and financial assistance and he thanks UNAM and CONACYT (Mexico) for sabbatical leave and financial support.

REFERENCES

Brucker, C. 1999 Structure and dynamics of the wake of bubbles and its relevance for bubble interaction. *Phys. Fluids* **11**, 1781–1796.

Clift, R., Grace, J. R. & Weber, M. E. 1978 *Bubbles, Drops, and Particles*. Academic.

Coutanceau, M. & Defaye, J. R. 1991 Circular cylinder wake configurations: a flow visualization survey. *Appl. Mech. Rev.* **44**, 255–305.

Crocker, J. C. & Grier, D. G. 1996 Methods of digital video microscopy for colloidal studies. *J. Colloid Interface Sci.* **179**, 298–310.

Crow, S. C. 1970 Stability theory for a pair of trailing vortices. *AIAA J.* **8**, 2172–2179.

Govardhan, R. & Williamson, C. H. K. 2000 Modes of vortex formation and frequency response of a freely vibrating cylinder. *J. Fluid Mech.* **420**, 85–130.

Hover, F. S., Techet, A. H. & Triantafyllou, M. S. 1998 Forces on oscillating uniform and tapered cylinders in crossflow. *J. Fluid Mech.* **363**, 97–114.

Jauvtis, N. & Williamson, C. H. K. 2004 The effect of two degrees of freedom on vortex induced vibration at low mass and damping. *J. Fluid Mech.* **509**, 23–62.

Jenny, M., Dusek, J. & Bouchet, G. 2004 Instabilities and transition of a sphere falling or ascending freely in a Newtonian fluid. *J. Fluid Mech.* **508**, 201–239.

Johnson, T. A. & Patel, V. C. 1998 Flow past a sphere up to a Reynolds number of 300. *J. Fluid Mech.* **378**, 19–70.

Karamanev, D. G. 1994 Rise of gas bubbles in quiescent liquids. *AIChE J.* **40**, 1418–1421.

Karamanev, D. G., Chavarie, C. & Mayer, R. C. 1996 Dynamics of the free rise of a light solid sphere in liquid. *AIChE J.* **42**, 1789–1792.

Karamanev, D. G. & Nikolov, L. N. 1992 Free rising spheres do not obey Newton's law for free settling. *AIChE J.* **38**, 1843–1846.

Lee, S. 2000 A numerical study of the unsteady wake behind a sphere in a uniform flow at moderate Reynolds numbers. *Comput. Fluids* **29**, 639–667.

Lee, T. & Budwig, R. 1991 A study of the effect of aspect ratio on vortex shedding behind circular-cylinders. *Phys. Fluids* A **2**, 309–315.

Lighthill, J. 1986 Wave loading on offshore structures. *J. Fluid Mech.* **173**, 667–681.

Mittal, R. 2000 Response of the sphere wake to freestream fluctuations. *Theor. Comput. Fluid Dyn.* **13**, 397–419.

Mittal, S. 2001 Computation of three-dimensional flows past circular cylinder of low aspect ratio. *Phys. Fluids* **13**, 177–191.

Nakamura, I. 1976 Steady wake behind a sphere. *Phys. Fluids* **19**, 5–8.

Natarajan, R. & Acrivos, A. 1993 The instability of the steady flow past spheres and disks. *J. Fluid Mech.* **254**, 323–344.

Norberg, C. 1994 An experimental investigation of the flow around a circular-cylinder – influence of aspect ratio. *J Fluid Mech.* **258**, 287–316.

Ormieres, D. & Provansal, M. 1999 Transition to turbulence in the wake of a sphere. *Phys. Rev. Lett.* **83**, 80–83.

Pan, T.-W. 1999 Numerical simulation of the motion of a ball falling in an incompressible viscous fluid. *C. R. Acad. Sci. Paris* IIb **327**, 1035–1038.

Provansal, M., Schouveiler, L. & Leweke, T. 2004 From the double vortex street behind a cylinder to the wake of a sphere. *Eur. J. Mech. B* **23**, 65–80.

Schouveiler, L. & Provansal, M. 2002 Self-sustained oscillations in the wake of a sphere. *Phys. Fluids* **14**, 3846–3854.

Taneda, S. 1956 Experimental investigation of the wake behind a sphere at low Reynolds numbers. *J. Phys. Soc. Japan* **4**, 1104–1108.

Tomboulides, A. G. & Orszag, S. A. 2000 Numerical investigation of transitional and weak turbulent flow past a sphere. *J. Fluid Mech.* **416**, 45–73.

Widnall, S. E., Bliss, D. & Zalay, A. 1971 Theoretical and experimental study of the stability of the vortex pair. In *Aircraft Wake Turbulence and its Detection*. Plenum.

Williamson, C. H. K. 1996 Vortex dynamics in the cylinder wake. *Annu. Rev. Fuid Mech.* **28**, 477–539.

Williamson, C. H. K. & Roshko, A. 1988 Vortex formation in the wake of an oscillating cylinder. *J. Fluids Struct.* **2**, 355–381.

Zdravkovich, M. M. 1997 *Flow Around Circular Cylinders. Volume I: Fundamentals*. Oxford University Press.

Zdravkovich, M. M. 2002 *Flow Around Circular Cylinders. Volume II: Applications*. Oxford University Press.